Anharmonicity of the acoustic modes of graphene

R. Ramírez* and C. P. Herrero

Instituto de Ciencia de Materiales de Madrid (ICMM), Consejo Superior de Investigaciones Científicas (CSIC), Campus de Cantoblanco, 28049 Madrid, Spain

(Received 27 April 2020; revised manuscript received 5 June 2020; accepted 9 June 2020; published 23 June 2020)

The anharmonicity of the acoustic phonon dispersion of graphene has been studied by the harmonic linear response (HLR) approach at finite temperature. This is a nonperturbative method based on the linear response of the system to applied forces, as derived from equilibrium computer simulations. Anharmonic shifts are analyzed in the long-wavelength limit at room temperature, with emphasis on the effect of applied tensile or compressive in-plane stress. The simulation results are compared with available analytical models, based either on first-order perturbation theory or on a description by anomalous exponents. The simulations show better agreement to the expectations of the perturbational approach. The effect of temperature and zero-point vibrations on the acoustic out-of-plane anharmonic shifts of graphene are briefly reviewed.

DOI: 10.1103/PhysRevB.101.235436

I. INTRODUCTION

Geim and Novoselov made the seminal discovery that graphene, a two dimensional, one-atom width layer found as stacks in graphite, can be manipulated as a stable planar layer [1]. Graphene flakes have been characterized by optical, electrical, mechanical, and transport methods [2,3]. Two-dimensional (2D) crystalline solids were expected to lose their long-range ordering as a consequence of spatial atomic fluctuations caused by zero-point vibrations and temperature [4]. The unexpected stability of crystalline flat membranes, like graphene, has been explained by *anharmonic effects*, caused by the coupling between in-plane and out-of-plane vibrational modes [5,6].

The simplest treatment of anharmonic effects in solids is the quasiharmonic approximation (QHA). This approach considers that the angular frequency ω of each phonon may change with the volume of the crystal (or in-plane area in 2D solids) but does not depend explicitly on temperature. The volume dependence is described by the Gruneisen constants γ_ω and the harmonic limit implies $\gamma_\omega = 0$. The usual quasiharmonic behavior corresponds to values $\gamma_\omega > 0$, but certain solids display $\gamma_\omega < 0$ for some phonons. Negative Gruneisen constants appear in solids with tetrahedral coordination, as diamond, silicon, quartz, or ice Ih, and also in anisotropic structures such as graphite and graphene [7,8]. A set of long-wavelength acoustic modes with $\gamma_\omega < 0$ is the origin of the negative thermal expansion of solids at low temperatures. The negative thermal expansion of graphene has been studied both experimentally and theoretically by the QHA and perturbation theory methods, as well as by computer simulations [8–11]. The shortcomings of the QHA to describe anharmonic effects in graphene is evident by its incapability to reproduce the crossover from a negative to a positive thermal expansion coefficient as the temperature increases [8].

Anharmonic effects beyond those described by the QHA are often called *explicitly anharmonic* [12]. They are caused by higher-than-quadratic terms in the potential energy. They produce frequency shifts, with respect to the harmonic limit, that depend explicitly on the temperature. The explicit anharmonicity of the ZA out-of-plane acoustic modes of graphene has been analyzed by using perturbation theory [6,11,13–15]. The main perturbational result is that, in the long-wavelength limit, the harmonic (H) acoustic ZA dispersion $\rho\omega_{\rm ZA}^2 = \kappa k^4$ of an *unstressed* graphene layer is renormalized to $\rho\omega_{\rm ZA}^2 = \sigma k^2 + \kappa k^4$. Here ρ is the surface density, κ is the bending rigidity, σ is the fluctuation tension, and k is the modulus of the wave vector $\mathbf{k}$. The tension σ defines the lowest-order wave vector dependence of the spatial out-of-plane fluctuations [16,17].

Two physical consequences are derived from the explicit anharmonicity of the ZA phonons in graphene. The first is related to the mean quadratic amplitude h^2 of the out-of-plane modes. In the *harmonic limit,* the quadratic amplitude increases linearly with the number of layer atoms $h^2 \sim N$, leading to a catastrophic divergence in the thermodynamic limit. However, the anharmonic renormalization displays a less critical divergence as $h^2 \sim \ln N$, explaining an increased stabilization of the flat layer. The second consequence is that the acoustic sound velocity $v_{\rm ZA} = (\partial\omega_{\rm ZA}/\partial k)_{k=0}$ vanishes in the harmonic limit, but becomes finite by explicit anharmonicity [14,15].

An alternative theoretical framework to explain the stability of a flat graphene layer is based on the description of the explicit anharmonicity by a k-dependent renormalization of the bending constant κ, giving rise to an acoustic ZA dispersion $\rho\omega_{\rm ZA}^2 = \kappa k^{4-\eta}$. η is a positive *anomalous exponent* that was estimated as $\eta = 0.82$ within the self-consistent screening approximation [18]. The numerical analysis of out-of-plane amplitudes in several computer simulations of

*ramirez@icmm.csic.es

graphene provides values in a range $\eta = 0.67$–1.1 [5,19]. However, the exponent η is believed to be a universal quantity, so that the variability reported in computer simulation remains unexplained [2]. Within this model, the mean quadratic amplitude $h^2 \sim N^{1-(\eta/2)}$ becomes much smaller than the harmonic expectation, stabilizing the flat layer. However, the acoustic sound velocity v_{ZA} vanishes, in disagreement to the perturbation theory results.

The question about which model (perturbation theory vs anomalous exponent) provides better agreement to experiment has not been unambiguously answered, as neither the dispersion relation of the ZA modes in the long-wavelength limit nor the associated sound velocity have been measured yet. Several computer simulations published so far are interpreted in terms of the anomalous exponent model [5,19–22], but there are exceptions [23]. In spite of the absence of definite evidence, there seems to be a certain consensus that the anomalous exponent model is the correct one for graphene [2].

In this paper we study the explicit anharmonicity of the acoustic phonon dispersion bands of graphene (two in-plane and one ZA branches) using the empirical long-range carbon bond order (LCBOPII) model [24]. The harmonic linear response (HLR) method is a nonperturbative approach used to study *anharmonic* vibrations from the analysis of spatial trajectories generated by equilibrium simulations. The method was originally proposed in the framework of quantum path-integral (PI) simulations [25]. It has been recently applied to derive the dispersion bands of 2D solids such as a graphene monolayer, a graphene bilayer, and graphane [26]. The explicit anharmonicity derived by the HLR method will be compared to the expectations of the available analytical models (perturbation theory vs anomalous exponent).

The paper is organized as follows. The computational method for the calculation of the phonon dispersion of graphene is presented in Sec. II. The expectation of the QHA is discussed in Sec. III. The study of the explicit anharmonicity of the acoustic bands of graphene at 300 K as a function of the in-plane stress is found in Sec. IV. The comparison of simulation results and analytical models is the focus of Sec. V. Temperature and quantum effects in the anharmonicity of the out-of-plane modes of graphene are commented in Sec. VI. The paper closes with a summary.

II. COMPUTATIONAL METHOD

In this section, a minimum set of technical details is presented concerning the simulation method and the calculation of phonon dispersion relations in graphene. Further technical information can be found in Refs. [23,26].

A. MD simulations

Classical molecular dynamics (MD) simulations of graphene were performed in the $N\tau T$ ensemble at temperature $T = 300$ K and applied in-plane stress τ between -0.02 and 0.01 eV/Å^2. $\tau > 0$ ($\tau < 0$) implies compressive (tensile) stress. The interatomic forces were calculated with a realistic interatomic potential, namely, the so-called LCBOPII model. This is a long-range carbon bond order potential, fitted to *ab initio* electronic structure calculations, aiming at the description of carbon liquid and solid phases, first of all graphite and diamond, as accurately as possible [24]. It has been employed earlier to perform classical simulations of liquid carbon [27], diamond, graphite [24], and graphene layers [21,28,29]. It has been used to predict the carbon phase diagram comprising graphite, diamond, and the liquid, showing that the graphite-diamond transition line is in good agreement with experimental data [30]. The LCBOPII model has been found to give a good description of the elastic properties, such as the Young's modulus of graphene [28,31]. A brief account of the empirical LCBOPII model is presented in Appendix A.

The simulation cell was a rectangular one with $N = 8400$ carbon atoms and similar lengths ($L \sim 148$ Å) along the x and y axis in the plane of the layer. The in-plane area per atom is denoted as A_p. Periodic boundary conditions were applied to the simulation cell in the xy plane. The MD simulations of graphene were performed in the $N\tau T$ ensemble by allowing isotropic fluctuations of the in-plane area. The equations of motion, which are summarized in Appendix B, were integrated using different time steps for the fast and slow degrees of freedom [32]. The employed time step for the calculation of interatomic forces was $\triangle t = 1$ fs. For the time evolution of the thermostats and barostat variables we used a time step of $\triangle t/4$, as in earlier simulations [33]. The equilibration run comprised 10^5 MD steps. Trajectories with $S = 5 \times 10^4$ spatial configurations were stored for further analysis at equidistant intervals from a long simulation run with 10^7 MD steps. Long trajectories are mandatory for a reasonable sampling of the sluggish long-wavelengths acoustic modes.

B. Phonon dispersion calculation

The HLR method is a nonperturbative approach to obtain the phonon dispersion relations from the analysis of the spontaneous atomic fluctuations of the system, by either classical or quantum PI simulations. This method requires only spatial information (i.e., not atomic velocities). This is an advantage in PIMD simulations as the atomic velocities do not carry true physical information on the dynamics of the quantum particles [34]. The physical basis and applicability of this method to 2D solids has been explained in detail in Ref. [26]. For this reason, only a succinct sketch of the method is given here.

From the stored trajectory one needs to calculate the in-plane equilibrium positions of the cell atoms $\mathbf{r}_{\mathrm{eq},\alpha j}$. α is an index (1 or 2) that runs over the two basis atoms of a primitive cell, while j is an index running over all the basis atoms α in the simulation cell ($N/2$ α-type atoms). The equilibrium z coordinate of the atoms in the flat layer can be set as $z_{\mathrm{eq}} = 0$, without loss of generality.

If the instantaneous displacement vector of an atom from its average position $(\mathbf{r}_{\mathrm{eq},\alpha j}, z_{\mathrm{eq}})$ is denoted as $(X_{\alpha j}, Y_{\alpha j}, Z_{\alpha j})$, one needs to calculate symmetry adapted Bloch functions $\overline{X}_\alpha(\mathbf{k})$ with the displacement coordinates as

$$\overline{X}_\alpha(\mathbf{k}) = \sqrt{\frac{2m}{N}} \sum_{j=1}^{N/2} X_{\alpha j} \exp(i\mathbf{k}\mathbf{r}_{\mathrm{eq},\alpha j}), \tag{1}$$

where m is the carbon mass, and $\mathbf{k}$ is a wave vector commensurate with the employed simulation

cell [26]. The number of Bloch functions is 6, i.e., $[\overline{X}_1(\mathbf{k}), \overline{Y}_1(\mathbf{k}), \overline{Z}_1(\mathbf{k}), \overline{X}_2(\mathbf{k}), \overline{Y}_2(\mathbf{k}), \overline{Z}_2(\mathbf{k})]$, which corresponds to the number of vibrational bands in graphene. The covariance of symmetry adapted displacement coordinates is calculated as

$$\langle \overline{C}_\alpha(\mathbf{k})\overline{D}^*_\beta(\mathbf{k})\rangle = S^{-1}\sum_{s=1}^{S}(\overline{C}_\alpha(\mathbf{k})\overline{D}^*_\beta(\mathbf{k}))_s, \tag{2}$$

where s is a running index for the stored trajectories, C and D are any of the coordinates (X, Y, Z), and α and β are any of the basis atoms (1,2). The covariances form a 6×6 tensor $\chi(\mathbf{k})$. The jth eigenvalue $\Delta_j(\mathbf{k})$ of the tensor $\chi(\mathbf{k})$ provides an estimation of the angular frequency associated with the jth phonon branch of the 2D layer as [26]

$$\omega_j^2(\mathbf{k}) = \frac{k_B T}{\Delta_j(\mathbf{k})}, \tag{3}$$

where k_B is the Boltzmann constant. Within the grid of wave vectors $\mathbf{k}$ commensurate with the simulation cell, the two $\mathbf{k}$ vectors with largest wavelength, oriented along either the x or y directions, will be denoted as $\mathbf{k}_{\min}$. The modulus of these vectors is $k_{\min} = 2\pi/L$.

The phonon angular frequencies derived by the HLR method are obtained from the atomic fluctuations at the equilibrium volume of the solid at a given temperature. This implies that the volume dependence of the vibrational modes, i.e., the anharmonic effect described by a QHA approach, is automatically included in the HLR method. In addition, the HLR approach is able to describe anharmonic effects beyond those described by a QHA. For example, in Ref. [35] the HLR phonon frequencies of solid neon were compared with the QHA result as a function of temperature in a range between 5–25 K, and also with the harmonic approach. The error, with respect to the experimental data, of the harmonic phonon frequency of the longitudinal phonon at the point X of the Brillouin zone (BZ) of the fcc lattice amounts to 40%. The QHA phonon frequency was derived by diagonalization of the dynamic matrix at the equilibrium volume of the solid at each temperature. The QHA phonon frequency improves the harmonic result, but is still about 20% below the experimental data in the studied temperature range. However, the HLR result is off by less than 2%. Then the correlation between atomic fluctuations, as analyzed by the HLR approach, is sensitive to anharmonic effects that are absent in a QHA.

C. Phonon dispersion at 300 K

The phonon dispersion relations of graphene have been derived by the HLR method at 300 K and in-plane stresses τ in the range $[-0.02, 0.01]$ eV/Å^2. For $\tau = 0$, the frequencies $\omega_j(\mathbf{k})$ along the symmetry directions in the hexagonal Brillouin zone (BZ) are displayed as open circles in Fig. 1. The density of points in the $\mathbf{k}$ grid is determined by the size of the simulation cell and the shortest distance between $\mathbf{k}$ points amounts to $k_{\min} = 0.042$ Å^{-1}. The average in-plane area at 300 K is $A_p = 2.6162$ Å^2/atom. The harmonic phonon dispersion relations, as derived from the diagonalization of the dynamical matrix using a denser grid of $\mathbf{k}$ points, are displayed by closed circles. In the figure these points appear as a continuous line. The in-plane area corresponding to the minimum potential energy amounts to $A_p = 2.6189$ Å^2/atom. The phonon dispersion curves consist of three acoustic (A) and three optical (O) bands. The atomic displacement vectors of the phonons are either in-plane longitudinal (L), in-plane transverse (T), or out-of-plane (Z). The linear dispersion of the LA and TA modes in the long-wavelength limit ($k \to 0$), typical for the acoustic modes of 3D solids, contrasts with the k^2 dependence of the ZA mode in the harmonic approximation [36]. Differences between harmonic and HLR dispersion curves are due to anharmonic effects. We are particularly interested in the anharmonicity of the long wavelength acoustic region (LA, TA, and ZA branches), close to the special point Γ, a region shown by the inset of Fig. 1. The largest anharmonic effect in the dispersion relations at 300 K corresponds to a blueshift of the optical branches (LO and TO). This anharmonic effect has been studied in Ref. [26] with the conclusion that it is an artifact of the employed LCBOPII model.

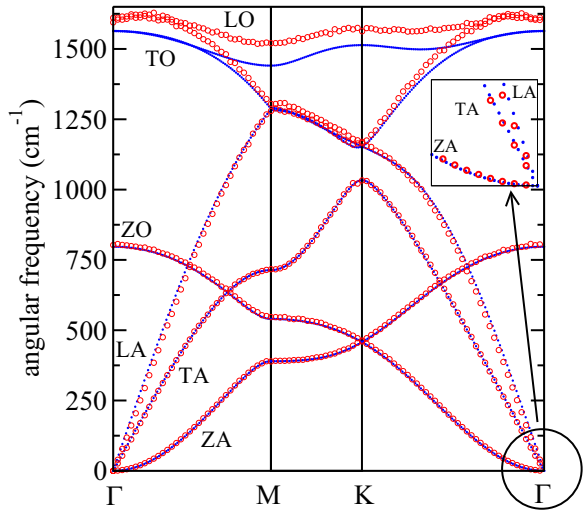

FIG. 1. The phonon dispersion relations of graphene at 300 K as derived by the HLR method with the LCBOPII model are displayed as open circles. The labels of the different branches are given. The inset shows the acoustic region around point Γ, which is studied in this work. The harmonic limit of the LCBOPII model, as derived from the diagonalization of the dynamical matrix, is displayed by closed circles.

III. ANHARMONICITY IN THE QHA

In this section, predictions of the QHA are presented for graphene, as derived with the employed LCBOPII model. The QHA analysis here focuses on the determination of the signs (+ or −) expected for the anharmonic shifts of the acoustic LA, TA, and ZA vibrational modes as a function of the applied in-plane stress and temperature. In Sec. IV the QHA expectation will be compared to the actual anharmonicity as derived by the HLR method. As a result of this comparison, it will be clear that the QHA does not provide a realistic description of the anharmonic shifts found for these modes. For this reason, the analysis of the QHA here is mainly done in qualitative terms.

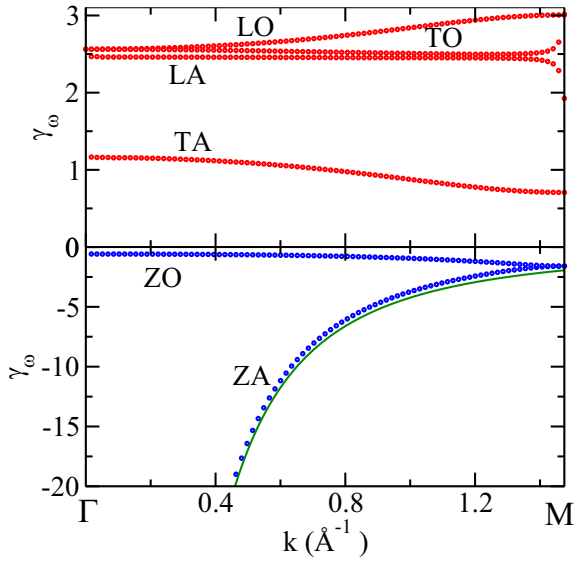

FIG. 2. The Gruneisen constants of the six phonon dispersion bands of graphene along the ΓM symmetry direction are shown by closed circles. The bands with z polarizations (ZO, ZA) display $\gamma_\omega < 0$. The continuous line is the long-wavelength limit of $\gamma_{\rm ZA}$, as given by Eq. (9) for $\tau = 0$. The data correspond to the LCBOPII model. Note the different vertical scales in the upper and lower parts of the figure.

The dependence of the vibrational frequencies ω with the in-plane stress τ and the temperature T is described within the QHA by the Gruneisen constants. The Gruneisen constant for a mode w is defined as

$$\gamma_\omega = -\frac{A_p}{\omega}\frac{\partial \omega}{\partial A_p}. \tag{4}$$

By considering the definition of the in-plane compressional modulus (the 2D analogous to the bulk modulus of 3D solids),

$$B = -A_p\frac{\partial \tau}{\partial A_p}, \tag{5}$$

the change of w with the in-plane stress τ is expressed as a function of the Gruneisen constant as

$$\frac{\partial \omega}{\partial \tau} = \frac{\partial \omega}{\partial A_p}\frac{\partial A_p}{\partial \tau} = \frac{\gamma_\omega \omega}{B}. \tag{6}$$

Analogously, the change of w with T can be deduced by considering the definition of γ_w and the thermal expansion coefficient $\alpha_T = A_p^{-1}\partial A_p/\partial T$ as

$$\frac{\partial \omega}{\partial T} = \frac{\partial \omega}{\partial A_p}\frac{\partial A_p}{\partial T} = -\gamma_\omega \omega \alpha_T. \tag{7}$$

The Gruneisen constants of graphene along the symmetry direction ΓM are presented in Fig. 2. γ_ω was calculated with Eq. (4) by a numerical differentiation of the harmonic frequencies of the LCBOPII model using a relative increase in the equilibrium area A_p of 0.2%. The LCBOPII results for γ_ω are in good agreement with the *ab initio* calculation of Ref. [8]. The vibrational bands LO, TO, LA, and TA display $\gamma_\omega > 0$, i.e., the usual behavior found in most solids. These bands exhibit (x, y) polarization. The two z bands (ZO, ZA) display however $\gamma_\omega < 0$.

TABLE I. Signs of the expected QHA shifts of the vibrational frequencies of the acoustic LA, TA, and ZA modes in graphene. + (−) indicates a blueshift (redshift) of the frequency of the modes. The last two columns give the actual anharmonic shifts as derived from the HLR approach in Sec. IV.

	QHA			HLR	
	γ_ω	$\frac{\partial\omega}{\partial T}$	$\frac{\partial\omega}{\partial\tau}$	$\frac{\partial\omega}{\partial T}$	$\frac{\partial\omega}{\partial\tau}$
LA/TA	>0	+	+	−	−
ZA	<0	−	−	+	−

The Gruneisen constants of the ZA modes diverge in the limit $k \to 0$. The QHA dispersion relation of the ZA band in the long-wavelength limit is given as [37]

$$\rho\omega_{\rm ZA}^2 = -\tau k^2 + \kappa k^4. \tag{8}$$

The k^2 term vanishes for an unstressed layer ($\tau = 0$) at $T \to 0$. By taking the τ derivative of the last expression and with the help of Eq. (6), one gets

$$\gamma_{\rm ZA} = \frac{B}{2\tau - 2\kappa k^2}. \tag{9}$$

The Gruneisen constant $\gamma_{\rm ZA}$ displays a k^{-2} divergence when $\tau = 0$, in agreement with Ref. [37]. The long-wavelength approximation for $\gamma_{\rm ZA}$ in Eq. (9) is plotted by a continuous line in Fig. 2, where we have used the bending constant ($\kappa = 1.5$ eV) and the in-plane stiffness ($B = 12.6$ eV/Å^2) corresponding to the harmonic limit at $\tau = 0$. The approximation for $\gamma_{\rm ZA}$ is rather realistic in the whole BZ.

The QHA predictions for the sign (+ or −) of the frequency shifts of the acoustic branches of graphene with both temperature T and in-plane stress τ are summarized in Table I. The results are derived from Eqs. (6) and (7). The signs of the temperature shifts presented in Table I correspond to the case where the thermal expansion coefficient in Eq. (7) is $\alpha_T < 0$, which is the expected QHA behavior when $\gamma_{\rm ZA} < 0$ [8].

IV. EXPLICIT ANHARMONICITY

In this section, the anharmonic shifts of the acoustic vibrational modes of graphene are analyzed by the HLR method. This method is sensitive to both the volume dependent quasiharmonic effect and the temperature dependent explicit anharmonicity. The preponderance of explicit anharmonicity will be identified by comparing the HLR results to the expectations of the QHA. First, the anharmonicity of the mode with largest wavelength of each band $\omega_j(\mathbf{k}_{\rm min})$ (j = LA, TA, and ZA) is studied. Second, the elastic coefficients of the layer are derived from the k dependence of the acoustic dispersion bands.

A. Acoustic modes with longest wavelengths

1. LA and TA modes

For the employed simulation cell size $k_{\rm min} = 2\pi/L = 0.042$ Å^{-1}. There are two wave vectors with modulus $k_{\rm min}$,

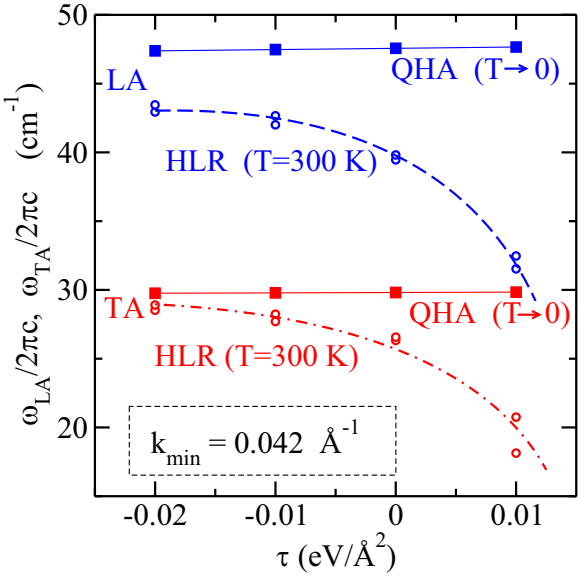

FIG. 3. Dependence of the angular frequency of the LA and TA phonons of graphene with the in-plane stress τ for the two **k** points with modulus $k_{\min}$. The HLR wave numbers at 300 K are given by open circles. The QHA results in the $T \to 0$ limit are shown as closed squares. Lines are guides to the eye.

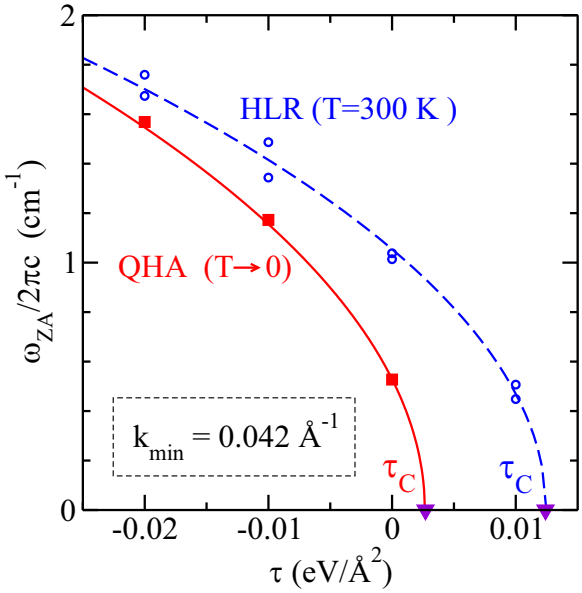

FIG. 4. Dependence of the angular frequency of the ZA phonons of graphene with the in-plane stress τ for the two **k** points with modulus $k_{\min}$. The HLR frequencies at 300 K are given by circles. The broken line is a two-parameter fit (d, τ_C) to $\omega_{ZA} = d(\tau_C - \tau)^{1/2}$. The QHA results in the $T \to 0$ limit, derived by diagonalization of the dynamical matrix, are shown as squares. The continuous line corresponds to Eq. (10). The filled triangles represent the critical stress τ_c, where the soft mode $\omega_{ZA}(k_{\min})$ becomes unstable.

oriented along the x and y axes [26]. The angular frequency $\omega_j(\mathbf{k}_{\min})$ for the in-plane polarized bands (j = LA and TA) are displayed in Fig. 3 as a function of the in-plane stress. The open circles show the HLR results at 300 K. The results for the **k** points $(k_{\min}, 0)$ and $(0, k_{\min})$ should be nearly identical, apart from the statistical error of the simulation, as the layer appears isotropic in the long-wavelength limit. At 300 K, one observes a sharp redshift of the LA/TA frequencies as the layer is compressed (τ increases), which is indicated with a negative sign in the HLR column ($\partial\omega/\partial\tau$) of Table I.

In a classical $T \to 0$ limit, the temperature dependent explicit anharmonicity vanishes, and the QHA becomes exact. This is only true in a classical limit. In the real world, there appears explicit anharmonicity even at $T \to 0$, as consequence of the zero-point vibration. In Fig. 3 we have plotted the QHA frequencies at $T \to 0$ (closed squares). These values were derived by numerical diagonalization of the dynamical matrix with the equilibrium area at $T \to 0$ for each τ. The QHA angular frequencies display a small blueshift as the in-plane stress τ increases (see Table I). This result contrasts with the redshift revealed by the HLR method.

In the QHA, the frequency shift for the LA/TA modes is positive (blueshift) for rising temperature (see Table I). However, one finds that the HLR frequencies at 300 K are redshifted with respect to the $T \to 0$ limit. This behavior agrees with the anharmonicity derived by perturbation theory for the in-plane LA/TA modes [6]. Thus, the QHA alone is unable to predict correctly even the sign of the frequency shifts for the LA/TA modes as a function of either the temperature or the in-plane stress. This analysis points out the importance of the explicit anharmonicity for the long-wavelength LA/TA modes in graphene.

2. ZA mode

In the low temperature limit ($T \to 0$), the dispersion of the ZA mode for long wavelengths is given in the QHA by Eq. (8). For the **k** vectors with modulus $k_{\min}$, one gets

$$\omega_{ZA} = k_{\min}\left(\frac{\tau_C - \tau}{\rho}\right)^{1/2}. \tag{10}$$

For the cell with $N = 8400$ atoms, the critical stress $\tau_C = \kappa k_{\min}^2 = 3 \times 10^{-3}$ eV/Å^2. The critical stress τ_C signals the point where the phonon mode becomes soft and its angular frequency vanishes, $\omega_{ZA}(k_{\min}) = 0$. The angular frequency $\omega_{ZA}(k_{\min})$ as a function of τ given by Eq. (10) is plotted in Fig. 4 as a continuous line. The open squares were calculated by diagonalization of the dynamical matrix for the area A_p in equilibrium at $T \to 0$ for given stress τ. As τ increases up to the critical stress τ_C, the mode $\omega_{ZA}(k_{\min})$ becomes soft, and the finite flat layer becomes mechanically unstable. The instability leads to a static deformation via sinusoidal wrinkles with wave vector $\mathbf{k}_{\min}$ [38,39].

At 300 K, the HLR angular frequencies $\omega_{ZA}(k_{\min})$ are displayed as a function of τ in Fig. 4 (open circles). The ZA phonons are blueshifted with respect to the $T \to 0$ limit. This contrasts with the redshift found for the LA/TA modes by rising temperature in Fig. 4. The blueshift for the ZA modes implies that the critical stress τ_C increases with temperature. In other words, the mechanical stability of the flat layer increases as temperature rises. The critical stress amounts to $\tau_C = 1.2 \times 10^{-2}$ eV/Å^2 at 300 K. It is important to recall that the value of τ_C displays a significant finite size effect, as τ_C depends on $k_{\min} = 2\pi/L$. The calculation of the critical

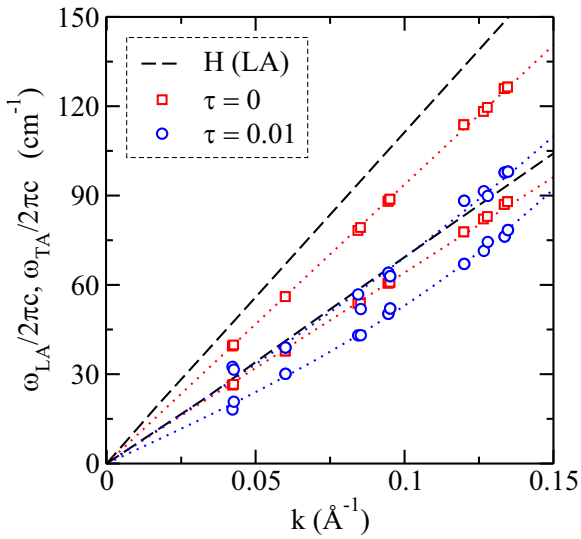

FIG. 5. LA and TA dispersion relations of graphene at in-plane stress $\tau = 0$ (open squares) and 0.01 eV/Å^2 (open circles). The two bands can be distinguished as the slope of the LA branch is larger. The dotted lines are least square fits of the simulation data to the analytic function in Eq. (11). The harmonic result at $\tau = 0$ is displayed by broken lines. At the compressive stress $\tau = 0.01$ eV/Å^2 the layer is close to its limit of mechanical stability.

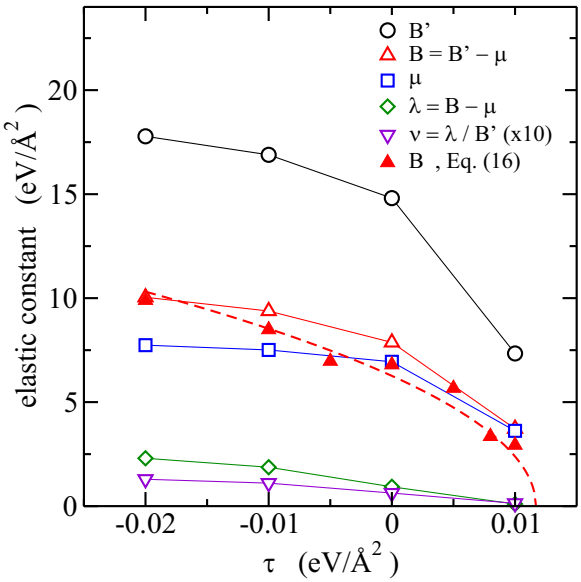

FIG. 6. In-plane stress dependence of the elastic constants of graphene at 300 K as derived from the slopes of the LA and TA phonon dispersion bands in the long-wavelength limit. Shown are the unilateral compressional modulus (B'), the shear modulus (μ), the in-plane compressional modulus (B), the Lamé's first coefficient (λ), and the Poisson's ratio (ν). The in-plane compressional modulus, derived from the fluctuation formula of the $N\tau T$ ensemble [Eq. (16)], is displayed by closed triangles. The broken line is a least squares fit of the closed triangles by Eq. (17). The continuous lines are guides to the eye.

stress for additional cell sizes with $N = 1500$ and 960 atoms, gives the result $\tau_C = 3.2 \times 10^{-2}$ and 5.4×10^{-2} eV/Å^2, respectively. These values imply that the finite size effect in τ_C has a N^{-1} dependence. The smaller the size of the simulation cell, the larger the stability of the flat morphology of the layer [40].

The shifts of the frequency of the ZA modes found by the HLR method by raising either the temperature (blueshift) or the in-plane stress (redshift) are summarized in Table I. The QHA predicts effects of opposite sign to the HLR method in the three acoustic bands of graphene (LA, TA, and ZA) when the temperature increases. However, the frequency shift of the ZA modes with the in-plane stress τ has, in the QHA, the same sign as in the HLR method.

B. LA, TA dispersions

The acoustic LA and TA phonon dispersions at two in-plane stresses ($\tau = 0$ and 0.01 eV/Å^2) are displayed for **k** vectors with $k < 0.15$ eV/Å^2 in Fig. 5. For comparison, the LA/TA harmonic phonon dispersions at $\tau = 0$ are also plotted. The anharmonicity caused by increasing the temperature and the in-plane stress is reflected by redshifts of the LA/TA dispersion curves with respect to the harmonic ones. Longitudinal (v_L) and transverse (v_T) sound velocities were derived from the slope of the dispersion curves in the long-wavelength limit ($k \to 0$) by a least squares fit of the function

$$\omega = (v^2k^2 + f\,k^3)^{1/2}, \tag{11}$$

where v is the sound velocity, and f is a fitting constant. For an isotropic elastic layer, the sound velocities are related to the elastic constants by

$$v_T = \left(\frac{\mu}{\rho}\right)^{1/2}, \tag{12}$$

$$v_L = \left(\frac{B'}{\rho}\right)^{1/2}, \tag{13}$$

where μ is the shear modulus (Lamé's second coefficient), and B' is the unilateral compressional modulus defined as [41]

$$B' = \lambda + 2\mu, \tag{14}$$

with λ being the Lamé's first coefficient. The in-plane compressional modulus is derived from μ and B' as

$$B = B' - \mu = \lambda + \mu, \tag{15}$$

while the Poisson's ratio can be obtained from $\nu = \lambda/B'$ [41]. The in-plane stress dependence of the elastic moduli μ, B', B, λ, and ν of graphene, as derived from the HLR analysis, is presented in Fig. 6. The Poisson's ratio has been scaled by a factor of 10 to be visible in the plot. All elastic constants display a sharp decrease with positive (compressive) in-plane stress. The Lamé's first coefficient λ takes the value 0.9 eV/Å^2 at $\tau = 0$, while it is reduced to $\lambda = 0.1$ eV/Å^2 at $\tau = 10^{-2}$ eV/Å^2. This compressive stress is close to the limit of mechanical stability of the employed simulation cell at 300 K, $\tau_C = 1.2 \times 10^{-2}$ eV/Å^2. The Poisson's ratio ν, proportional to the Lamé's first coefficient λ, remains positive

TABLE II. The in-plane area A_p, the elastic moduli μ and λ, the surface tension σ, and the bending rigidity κ of graphene as derived from $N\tau T$ simulations at $T = 300$ K and $N = 8400$ atoms. The harmonic limit is also given.

	τ (eV/Å^2)	A_p (Å^2/atom)	μ (eV/Å^2)	λ (eV/Å^2)	σ (eV/Å^2)	κ (eV)
H	0	2.6189	9.3	3.3	0	1.49
$N\tau T$	0.01	2.6103	3.6	0.1	−0.006	1.70
$N\tau T$	0	2.6162	6.9	0.9	0.008	1.70
$N\tau T$	−0.01	2.6195	7.5	1.8	0.017	1.69
$N\tau T$	−0.02	2.6223	7.7	2.3	0.025	1.71

in the whole range of studied in-plane stresses. In Table II we summarized the results for the Lamé's coefficients of graphene at 300 K.

Experimental phonon dispersion relations of a quasifree-standing graphene sample grown on Pt(111), characterized by the weakest graphene-metal interaction, have been determined by high-resolution electron energy loss spectroscopy (HREELS). The sound velocities derived from the slopes of the TA and LA branches were 14.0 and 22.0 km/s, respectively [31]. An optical technique to probe the acoustic TA and LA phonon branches of graphene near the Γ point by double resonant Raman scattering reported acoustic sound velocities of 12.9 and 19.9 km/s, respectively [42]. The sound velocities in Fig. 6 for the unstressed graphene layer ($\tau = 0$) are 12.1 and 17.7 km/s, respectively, in reasonable agreement to the previous experimental data.

It is interesting to compare the compressional modulus B (open triangles in Fig. 6) derived from the LA/TA phonon dispersion relations, to the value derived from the fluctuation formula corresponding to the $N\tau T$ ensemble [40,43],

$$B = \frac{A_p k_B T}{N \delta A_p^2}. \tag{16}$$

The quadratic deviation δA_p^2 is the ensemble average $\langle A_p^2 \rangle - \langle A_p \rangle^2$. The closed triangles in Fig. 6 display B calculated by the fluctuation formula at several in-plane stresses for MD simulations using cells with $N = 8400$ atoms. These MD results for the compressional modulus B seem to be systematically smaller than those derived via Eq. (15). This difference was already observed in Ref. [26] for simulations cells with $N = 960$ atoms, and was attributed to the out-of-plane fluctuations of the layer that make the layer lose a strict 2D character.

For a 2D solid approaching a mechanical instability, the compressional modulus is expected to display the following dependence with the in-plane stress τ (see Appendix C),

$$B = b(\tau_C - \tau)^{1/2}, \tag{17}$$

where b is a constant, and τ_C is the critical stress for the instability to occur. The broken line in Fig. 6 displays a least squares fit of Eq. (17) to the simulation data (closed triangles). The fitted parameters amount to $b = 58$ eV$^{1/2}$/Å and $\tau_C = 1.2 \times 10^{-2}$ eV/Å^2. This new independent estimation of the critical stress τ_C is in agreement with the value derived in Fig. 4 by studying the soft mode $\omega_{\rm ZA}(k_{\rm min})$ of the ZA band with the HLR method.

C. ZA dispersion

The ZA phonon band of graphene for wave vectors with $k < 0.2$ Å^{-1} is displayed as a function of the in-plane stress at a temperature of 300 K in Fig. 7. In Sec. IV A the anharmonic shifts found in the frequency of the ZA mode were a blueshift by rising temperature and a redshift as the in-plane stress increases (see Table I). The ZA dispersion band has been fitted to the expression

$$\rho\omega_{\rm ZA}^2 = \sigma k^2 + \kappa k^4 + d k^6, \tag{18}$$

where the surface tension σ, the bending rigidity κ, and d are fitting parameters. The least squares fit included all wave vectors with $k < 0.3$ Å^{-1}. In the QHA at $T \to 0$, the relation between the surface tension σ and the in-plane stress τ is $\sigma = -\tau$ [see Eq. (8)]. It is interesting to study to which extent the temperature dependent explicit anharmonicity modifies this QHA relation.

The results of the least squares fits are plotted by continuous lines in Fig. 7. The fluctuation tension σ_0 for the

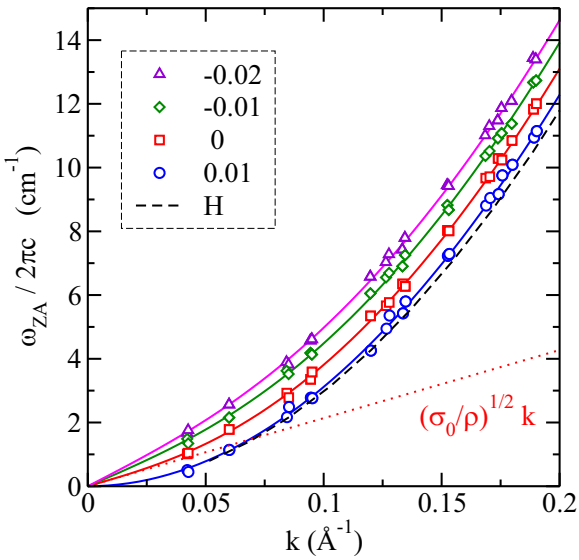

FIG. 7. ZA dispersion relations of graphene at 300 K as a function of the in-plane stress (τ) as derived with the LCBOPII model by the HLR method. The values of τ are in eV/Å^2. The continuous lines are the least squares fit of the simulation data to the analytic function in Eq. (18). The dotted line shows the linear term of the fitted function for $\tau = 0$ (open squares). The broken line is the harmonic limit of the LCBOPII model derived by diagonalization of the dynamical matrix at $\tau = 0$. At the compressive stress $\tau = 0.01$ eV/Å^2 the flat layer is close to its limit of mechanical stability.

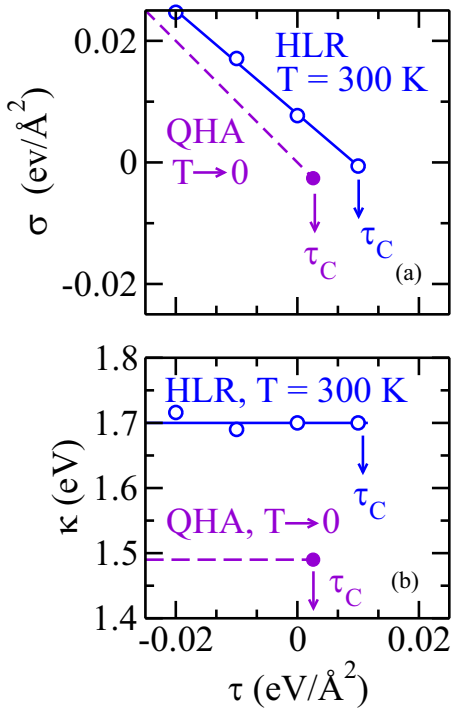

FIG. 8. (a) The fluctuation tension σ is displayed as a function of the in-plane stress τ. The broken line is the QHA at $T \to 0$ K, $\sigma = -\tau$. The open circles are results from the ZA dispersion relations derived by the HLR method at 300 K. The explicit anharmonicity of graphene is the origin that the curve at 300 K is shifted with respect to the $T \to 0$ limit. The critical stress τ_C corresponding to the employed cell size ($N = 8400$) is indicated by an arrow and a closed circle. τ_C is larger at 300 K than in the $T \to 0$ K limit. (b) In-plane stress dependence of the bending constant κ at 300 K and in the $T \to 0$ limit.

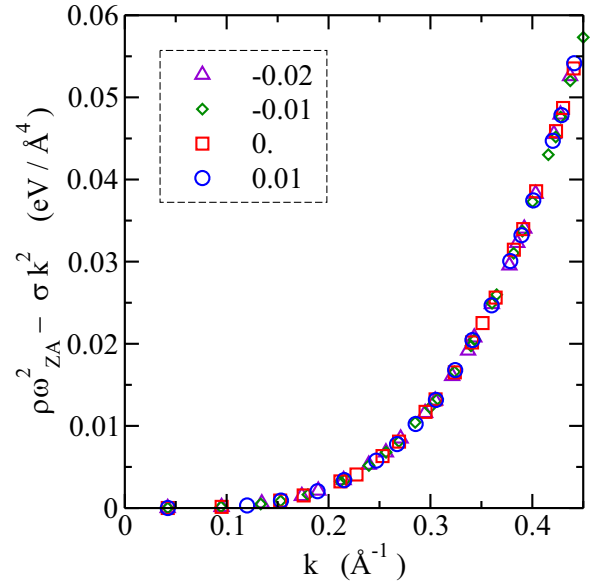

FIG. 9. The difference $\rho\omega_{\rm ZA}^2 - \sigma k^2$ is represented as a function of k for the four studied in-plane stresses. The values of τ are given in eV/Å^2. The results for the different stresses lie in the same curve.

unstressed layer ($\tau = 0$) is finite and amounts to $\sigma_0 = 8 \times 10^{-3}$ eV/Å^2, which translates into a finite sound velocity $v_{\rm ZA} = (\sigma_0/\rho)^{1/2} = 0.4$ km/s. The linear term $v_{\rm ZA}k$ of the ZA dispersion band at $\tau = 0$ is displayed by a dotted line in Fig. 7. The harmonic limit at $\tau = 0$, as derived from the diagonalization of the dynamical matrix, is shown by a broken line in Fig 7.

The values of the fitted parameters σ and κ are summarized in Table II and plotted as a function of the in-plane stress in Fig. 8. At given stress τ, the fluctuation tension σ is larger at 300 K than at $T \to 0$. The dependence of σ with τ at 300 K is linear. A least squares fit of the simulation results gives

$$\sigma = \sigma_0 - 0.9\tau. \tag{19}$$

This relation is a consequence of the temperature dependent explicit anharmonicity in graphene. The result contrast to the QHA relation $\sigma = -\tau$ at $T \to 0$. The bending rigidity κ is at 300 K larger than at $T \to 0$. κ remains nearly constant for the studied in-plane stresses, even at the compressive stress of 0.01 eV/Å^2, close to the critical stress. However, the other in-plane elastic moduli (B' and μ) and the fluctuation tension σ display a significant variation as a function of the in-plane stress τ.

At 300 K, the critical stress τ_C can be expressed with the help of Eqs. (18) and (19) as

$$\tau_C = \frac{\sigma_0 + \kappa k_{\rm min}^2}{0.9}. \tag{20}$$

and takes the value $\tau_C = 1.2 \times 10^{-2}$ for the fitted results of σ_0 and κ. This is in agreement with the value of τ_C derived at 300 K from the τ dependence of $\omega_{\rm ZA}(k_{\rm min})$ in Fig. 4.

For the range of in-plane stresses studied here, when τ changes, the effect in the ZA band is limited to the σk^2 term of Eq. (18). In Fig. 9 the difference $\rho\omega_{\rm ZA}^2 - \sigma k^2$ is displayed for the four simulated stresses and wave vectors with $k < 0.4$ Å^{-1}. The resulting points lie all in the same curve, being nearly indistinguishable.

V. COMPARISON TO ANALYTICAL MODELS

In this section, the simulations results for the ZA dispersion are compared with available analytical models. The prediction of the anomalous exponent model in the long-wavelength limit is a renormalization of the harmonic relation $\rho\omega_{\rm ZA}^2 = \kappa k^4$, resulting in the ZA phonon dispersion $\rho\omega_{\rm ZA}^2 = \kappa_A k^{4-\eta}$, with $\eta = 0.82$ being an anomalous exponent [5,18]. To quantify the agreement between this anharmonic model and the simulation results, we performed a two-parameter least squares fit (κ_A, α_A) of the points of the ZA bands shown in Fig. 7 to the function

$$\rho\omega_{\rm ZA}^2 = \kappa_A k^{\alpha_A}. \tag{21}$$

The fitted region is the interval $[k_{\rm min}, k_{\rm max}]$. While $k_{\rm min} = 0.042$ Å^{-1} is a fixed value, determined by the size of the simulation cell, $k_{\rm max}$ is reduced from 0.6 to 0.1 Å^{-1}. When $k_{\rm max} = 0.6$ Å^{-1}, the fit includes a large region with 314 **k** points. When $k_{\rm max} = 0.1$ Å^{-1}, the fit includes only the 10 **k** points with the longest wavelengths. The change in the fitted

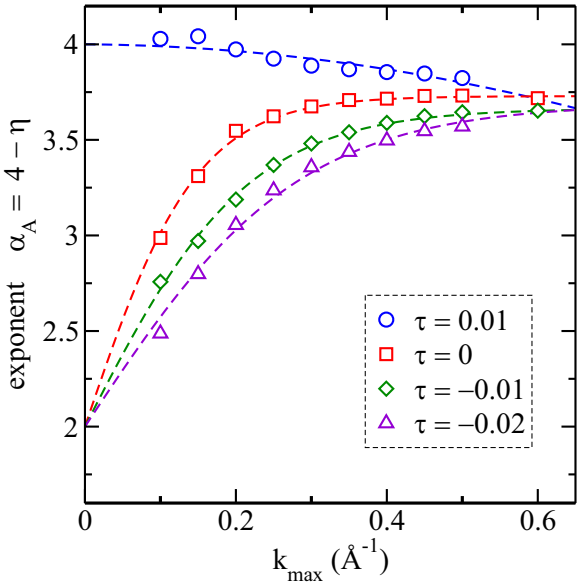

FIG. 10. Value of the exponent α_A derived from the fit of the simulation results for $\rho\omega^2_{ZA}$ to the anomalous exponent model $\kappa_A k^{\alpha_A}$ [see Eq. (21)]. The numerical fit is performed including wave vectors with modulus $k < k_{max}$. The results for the exponent α_A are shown as a function of k_{max} to quantify the convergence of the simulation results to the long-wavelength limit in Eq. (21). τ values are given in eV/Å^2. The lines are guides to the eye.

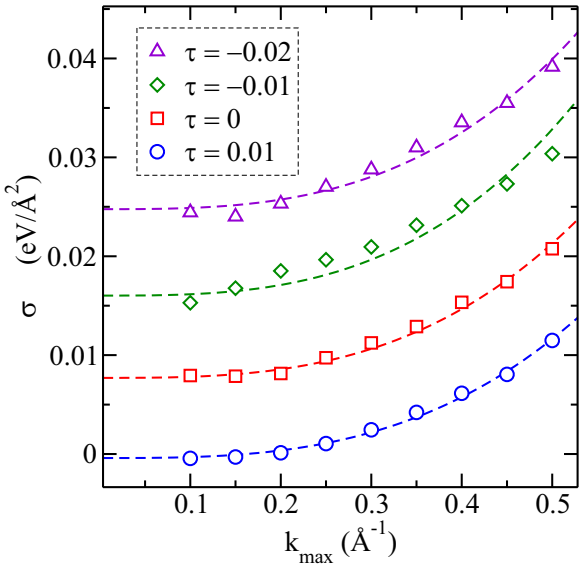

FIG. 11. Value of the surface tension σ from the fit of $\rho\omega^2_{ZA}$ to the prediction of the perturbation theory $\sigma k^2 + \kappa k^4$. The numerical fit is performed using only ZA angular frequencies with wave number modulus $k < k_{max}$. The results of σ are shown as a function of k_{max} to study the convergence of the model to the long-wavelength limit. τ values are given in eV/Å^2. The lines are guides to the eye.

parameters (κ_A, α_A) as the value of k_{max} decreases, allows us to visualize in which way the simulation results converge to the long-wavelength limit given by Eq. (21).

The result of the fitted exponent $\alpha_A = 4 - \eta$ as a function of k_{max} is presented in Fig. 10. When k_{max} is large the exponent α_A takes a value close to 4 for the four studied in-plane stresses, implying that $\rho\omega^2_{ZA}$ displays an overall dispersion that looks like k^4 when $k < 0.6$ Å^{-1}. As k_{max} decreases, the exponent α_A for the in-plane stresses $\tau \leqslant 0$ reduces monotonically towards lower values, which seem to converge in the long-wavelength limit to $\alpha_A = 2$, which would imply a long-wavelength dispersion for $\rho\omega^2_{ZA}$ with a dominant k^2 dependence. We do not see any qualitative difference between $\tau < 0$ (tensile stress) and $\tau = 0$ (unstressed layer), only that the convergence towards the limit $\alpha_A = 2$ is faster when the in-plane stress becomes more tensile. The data in Fig. 10 do not provide any evidence that the long-wavelength limit of the dispersion $\rho\omega^2_{ZA}$ when $\tau = 0$ should behave as $k^{3.2}$, as predicted by the anomalous exponent model.

For the compressive in-plane stress $\tau = 0.01$ eV/Å^2, the behavior of the exponent α_A is qualitatively different. As k_{max} becomes smaller the exponent α_A approaches 4. The interpretation of this behavior is that the compressed layer is close to its limit of mechanical stability, where there appears a soft phonon mode in the ZA band. This critical behavior is signalized by a $\rho\omega^2_{ZA}$ dispersion with k^4 dependence. We stress that here the k^4 dependence of $\rho\omega^2_{ZA}$ is a fingerprint of a soft phonon mode in the flat layer. It would be misleading to associate this k^4 dependence close to the critical stress τ_C, with an absence of anharmonic effects. In fact, the blueshift of the harmonic ZA modes at 300 K by the temperature dependent explicit anharmonicity, is compensated by an anharmonic redshift when the in-plane stress becomes more compressive (see Table I). At the critical stress τ_C, both anharmonic effects compensate each other, and the ZA dispersion takes the form of a k^4 dependence, signalizing the appearance of a soft ZA mode in the anharmonic layer.

Perturbation theory predicts the long-wavelength limit of the ZA band of graphene as $\rho\omega^2_{ZA} = \sigma k^2 + \kappa k^4$. We have tested this model against our simulation results by the same method used to check the anomalous exponent model. Then, a two-parameter least squares fit (σ, κ) of the ZA dispersion is made in the interval $[k_{min}, k_{max}]$. The result for the surface tension σ as a function of k_{max} is displayed for the studied in-plane stresses in Fig. 11. As k_{max} decreases, σ shows a monotonic convergence towards a constant value in the long-wavelength limit. At each studied in-plane stress τ, the relation $\sigma > -\tau$ is satisfied. This result differs from the QHA expectation $\sigma = -\tau$, because it is a consequence of explicit anharmonicity.

Note that for the compressive stress $\tau = 0.01$ eV/Å^2, σ is negative. For finite size simulation cells, where $k_{min} = 2\pi/L$ is finite, the ZA vibrational mode with lowest frequency $\rho\omega^2_{ZA}(k_{min}) = \sigma k^2_{min} + \kappa k^4_{min}$ may be positive, even if $\sigma < 0$. It is at the critical stress τ_C that this mode becomes soft, $\rho\omega^2_{ZA}(k_{min}) = 0$, and the flat surface morphology becomes mechanically unstable. In the thermodynamic limit $N \to \infty$, the mechanical instability would correspond to a vanishing value of the fluctuation tension ($\sigma = 0$), but for finite size cell the soft mode appears at negative values of the surface tension $\sigma < 0$.

VI. TEMPERATURE AND QUANTUM EFFECTS

The analysis of the anharmonicity of the acoustic modes in graphene at 300 K has been presented in the classical limit,

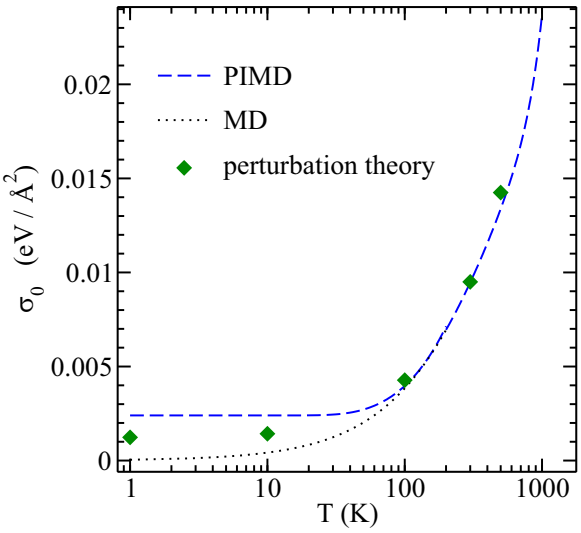

FIG. 12. Temperature dependence of the fluctuation tension σ_0 of graphene at in-plane stress $\tau = 0$. The broken line is a fit of the quantum PIMD results with a simulation cell with $N = 960$ atoms. The dotted line represents the corresponding results in the classical limit. Both results were taken from Ref. [38]. The filled diamonds are the values of σ_0 derived from perturbation theory in the quantum limit in Ref. [11].

using a relatively large simulation cell $N = 8400$ atoms, and very long simulations runs. With these conditions, quantum PI simulations at low temperature would require an enormous computational effort. In a recent paper we have presented classical and quantum PI simulations of graphene with a smaller simulation cell $N = 960$ atoms [38]. The quantum PIMD simulations were performed with in-plane stress $\tau = 0$ and temperatures in the range 25–1000 K. The smaller simulation cell implies that the wave vector with smallest modulus is $k_{\min} = 0.12$ Å^{-1}, i.e., about three times larger than that one corresponding to a cell with $N = 8400$ atoms. The study of the long-wavelength limit of the dispersion curves is less accurate with smaller cells, due to the cutoff of all collective vibrations with wavelengths larger than the cell dimension.

Nevertheless, the analysis of the long-wavelength limit of the ZA band in Ref. [38] using a smaller cell is in good in agreement with the analysis made in this paper. The fluctuation tension σ_0 at 300 K was of 8.7 ± 0.8 meV/Å^2 with $N = 960$ atoms, similar to our present result with a larger simulation cell ($\sigma_0 = 8$ meV/Å^2). In the classical limit σ_0 increases monotonously with temperature. The increase is a consequence of the explicit anharmonicity and vanishes at $T \to 0$ in a classical limit. The main quantum effect in the value of the fluctuation tension σ_0 is that the anharmonicity is finite even at $T \to 0$, as a consequence of the zero-point vibration. The extrapolated value at $T \to 0$ is $\sigma_0 \sim 2.5$ meV/Å^2 in the quantum case [38].

Further evidence of the agreement between our simulation results and perturbation theory is presented in Fig. 12. We have plotted the fit of the classical and quantum simulation results for σ_0 as a function of temperature, as derived in Ref. [38] with a simulation cell with $N = 960$ atoms. The temperature is presented in logarithmic scale to highlight the difference between classical and quantum results. This difference is significant only at temperatures below 100 K. In addition, the results for the fluctuation tension σ_0, which were derived in the quantum limit from perturbation theory, are also plotted in Fig. 12 [11]. The absence of any fitting parameter in this comparison between simulation and perturbation theory results provides further evidence for their striking agreement.

VII. SUMMARY

The anharmonicity of the acoustic phonon dispersion of graphene has been studied in the long-wavelength limit with the HLR method. This approach is based on the study of the correlation between the fluctuations of atomic positions from their equilibrium values by means of computer simulations. We have studied the phonon dispersion relations of graphene at 300 K and at various in-plane stresses, from a tensile stress of -0.02 eV/Å^2 to a compressive stress of 0.01 eV/Å^2. The latter is close to the mechanical stability limit of the flat layer, where the phonons of the ZA dispersion band at Γ become soft and cause the morphology of the flat layer to change by formation of static sinusoidal wrinkles. The simulations were performed at 300 K in the classical limit, which is a reasonable approach for the acoustic phonon vibrations in the long-wavelength limit. These are the modes having the lowest vibrational energies in the solid.

The QHA analysis of the LA/TA vibrational bands shows that this approach is unable to predict the anharmonicity found for these modes. The frequency of the long-wavelength limit of the LA/TA bands is predicted by the QHA to be blueshifted as either the temperature T or the in-plane stress τ increases. However, the HLR approach shows that the LA/TA frequencies are redshifted by raising either T or τ. This is a consequence of the explicit anharmonicity of these modes. The redshift of the LA/TA vibrational bands with rising temperature found in the simulation is in agreement with the prediction of perturbation theory [6].

The analysis of the long-wavelength limit of the ZA band reveals that the QHA is unable to predict the blueshift of the frequency of these modes by increasing temperature. This blueshift is an explicit anharmonic effect with deep influence in the physical properties of the layer. It is responsible for an increase in the mechanical stability of the flat layer. Both zero-point atomic vibrations and a rise in temperature produce a blueshift of the ZA band in the long-wavelength limit. However, a (compressive) increase of the in-plane stress τ of the layer produces a redshift of the frequency of the ZA modes. This anharmonic effect has a different sign than that one caused by temperature. Therefore, the increased mechanical stability of the flat layer, caused by an increase in T, can be compensated by the opposite effect of raising the in-plane stress. An important conclusion is that for an unstressed graphene membrane ($\tau = 0$) this compensation is not perfect, and the layer displays a small but finite fluctuation tension ($\sigma_0 > 0$) that determines the dispersion relation of the ZA band in the long-wavelength limit as $\rho\omega_{\rm ZA}^2 = \sigma_0 k^2$.

The simulation results for the long-wavelength limit of the ZA band have been compared with the predictions of two analytical models: perturbation theory and the anomalous exponent model. Our results are in good agreement with

perturbation theory, which predicts a finite fluctuation tension ($\sigma_0 > 0$) in the ZA band and a redshift of angular frequencies in the LA/TA bands caused by finite temperature and zero-point vibrations. The anomalous exponent model predicts a vanishing sound velocity of the ZA phonons in the unstressed layer that is not confirmed by our simulations.

ACKNOWLEDGMENTS

This work was supported by the Ministerio de Ciencia e Innovación (Spain) through Grant No. PGC2018-096955-B-C44. We thank the support of J. H. Los in the implementation of the LCBOPII model.

APPENDIX A: LCBOPII POTENTIAL

The total binding energy ϕ for a system consisting of N carbon atoms is defined with the LCBOPII empirical potential as [24]

$$\phi = \frac{1}{2}\sum_{i=1}^{N}\sum_{j=1}^{N}\left[S_{\rm sr}^{\rm down}(d_{ij})V^{\rm sr}(d_{ij}) + S_{\rm lr}^{\rm up}(d_{ij})V^{\rm lr}(d_{ij}) + \frac{1}{Z_i^{\rm mr}}S_{\rm mr}^{\rm up}(d_{ij})V^{\rm mr}(d_{ij})\right], \tag{A1}$$

where $V^{\rm sr}(d_{ij})$ describes short-range and covalent interactions, $V^{\rm lr}(d_{ij})$ accounts for long-range nonbonded interactions, and $V^{\rm mr}(d_{ij})$ represents the remainder of bonded (attractive) interactions between atoms at middle-range distances. d_{ij} is the interatomic distance between atoms i and j. The prefactor $1/Z_i^{\rm mr}$ takes into account many-body effects, with $Z_i^{\rm mr}$ being an effective middle-range coordination number of atom i. The switch functions $S_{sr}^{\rm down}$, $S_{\rm lr}^{up}$, and $S_{\rm mr}^{\rm up}$ provide a smooth connection between the various interaction contributions. The short-range interaction $V^{\rm sr}(d_{ij})$ vanishes at distances $d_{ij} > 2.2$ Å and describes both repulsive and attractive pair potentials. The attractive term depends on bond order factors that take into account many-body effects such as conjugation, presence of antibonding states, and torsion. The long-range interaction $V^{\rm lr}$ cuts off smoothly long-range interactions beyond 6 Å, while the middle-range attractive interactions $V^{\rm lr}$ depend on bond angles and on the presence of dangling bonds. For a detailed account of the analytical structure and parameters of this empirical potential we refer to the original work in Ref. [24]. According to previous simulations [44], the torsion parameters of the original LCBOPII model were slightly modified to increase the bending constant of the graphene layer from $\kappa = 0.8$ to 1.5 eV at $T \to 0$. The last value displays better agreement to experimental data and *ab initio* calculations [45].

In our MD simulations of graphene we have derived the potential energy ϕ of the layer with the LCBOPII model. The atomic forces of the graphene configurations,

$$(F_{xi}, F_{yi}, F_{zi}) = \left(-\frac{\partial\phi}{\partial x_i}, -\frac{\partial\phi}{\partial y_i}, -\frac{\partial\phi}{\partial z_i}\right), \quad i = 1, \ldots N, \tag{A2}$$

were calculated analytically with the LCBOPII potential, as well as the total derivative of the potential energy with respect the in-plane area of the simulation cell $d\phi/dA$. This derivative is defined by the change of the potential energy of the simulation cell upon an uniform isotropic strain in the xy plane. These quantities are required in the dynamic equations used to sample the $N\tau T$ ensemble.

APPENDIX B: DYNAMIC EQUATIONS FOR THE $N\tau T$ ENSEMBLE

The dynamic equations that generate the $N\tau T$ ensemble are reviewed here from the original literature in Refs. [32,46–49]. In order to produce the isothermal-isobaric ensemble, the in-plane area of the simulation cell $A = NA_p$ is permitted to undergo isotropic fluctuations. The employed extended system scheme treats as dynamic variables the atomic positions (x_i, y_i, z_i) and momenta (p_{xi}, p_{yi}, p_{zi}), with $i = 1, \ldots, N$, the in-plane area A, and the momentum associated with the logarithm of the in-plane area p_A. In addition, chains of Nosé-Hoover thermostats are employed to generate the thermal fluctuations of the distributed positions (x_i, y_i, z_i), and momenta (p_{xi}, p_{yi}, p_{zi}). An additional chain of thermostats is coupled to the "barostat" to control the area fluctuations. The equations of motion are [48,49]

$$\dot{x}_i = \frac{p_{xi}}{m} + \frac{p_A}{W}x_i, \tag{B1}$$

$$\dot{z}_i = \frac{p_{zi}}{m}, \tag{B2}$$

$$\dot{p}_{xi} = F_{xi} - \left(1 + \frac{1}{N}\right)\frac{p_A}{W}p_{xi} - \frac{p_{\xi xi1}}{Q}p_{xi}, \tag{B3}$$

$$\dot{p}_{zi} = F_{zi} - \frac{p_{\xi zi1}}{Q}p_{zi}, \tag{B4}$$

$$\dot{A} = \frac{2Ap_A}{W}, \tag{B5}$$

$$\dot{p}_A = 2A(\tau_{\rm int} - \tau) + \frac{1}{N}\sum_{i=1}^{N}\left(\frac{p_{xi}^2 + p_{yi}^2}{m}\right) - \frac{p_{\beta 1}}{Q_\beta}p_A, \tag{B6}$$

$$\dot{\xi}_{xij} = \frac{p_{\xi xij}}{Q}, \tag{B7}$$

$$\dot{p}_{\xi xi1} = \left(\frac{p_{xi}^2}{m} - k_BT\right) - p_{\xi xi1}\frac{p_{\xi xi2}}{Q}, \tag{B8}$$

$$\dot{p}_{\xi xij} = \left(\frac{p_{\xi xi(j-1)}^2}{Q} - k_BT\right) - p_{\xi xij}\frac{p_{\xi xi(j+1)}}{Q}, \quad 1 < j < M, \tag{B9}$$

$$\dot{p}_{\xi xiM} = \left(\frac{p_{\xi xi(M-1)}^2}{Q} - k_BT\right), \tag{B10}$$

$$\dot{\beta}_j = \frac{p_{\beta j}}{Q_\beta}, \tag{B11}$$

$$\dot{p}_{\beta 1} = \left(\frac{p_A^2}{W} - k_BT\right) - p_{\beta 1}\frac{p_{\beta 2}}{Q_\beta}, \tag{B12}$$

$$\dot{p}_{\beta j} = \left(\frac{p^2_{\beta(j-1)}}{Q_\beta} - k_B T\right) - p_{\beta j}\frac{p_{\beta(j+1)}}{Q_\beta}, \quad 1 < j < M, \tag{B13}$$

$$\dot{p}_{\beta M} = \left(\frac{p^2_{\beta(M-1)}}{Q_\beta} - k_B T\right). \tag{B14}$$

The equations of motion for the (y_i, p_{yi}) phase-space coordinates are identical to those given for (x_i, p_{xi}) upon changing the subindex x by y. m is the carbon mass and W is the mass of the barostat, which is coupled to the in-plane (x_i, p_{xi}) and (y_i, p_{yi}) phase-space coordinates. There are $3NM$ thermostats $(\xi_{xij}, \xi_{yij}, \xi_{zij})$, with mass Q and momentum $(p_{\xi xij}, p_{\xi yij}, p_{\xi zij})$, with $j = 1, \ldots, M$. Each of the $3N$ atomic momentum coordinates is coupled to a different chain of M Nosé-Hoover thermostats. The equations of motion for $(\xi_{yij}, p_{\xi yij})$ and $(\xi_{zij}, p_{\xi zij})$ are identical to those given for $(\xi_{xij}, p_{\xi xij})$ after changing the subindex x by y or z, respectively. This massive thermostatting of the system is mandatory for MD path-integral simulations to avoid ergodicity problems. For classical MD simulations it would be equally appropriate to use a unique thermostat chain for all the atoms. The only reason for using the massive thermostatting here is that the additional computational cost is low and thus the same homemade computer code can be used for both classical MD simulations and quantum PIMD simulations. The barostat is coupled to a chain of M thermostats β_j with mass Q_β and momentum $p_{\beta j}$. The graphene simulations presented here were done with $M = 4$, $Q = 2 \times 10^7$ eV fs^2, $Q_\beta = 2 \times 10^9$ eV fs^2, and $W = 3.2 \times 10^{15}$ eV fs^2. The internal in-plane stress is

$$\tau_{\rm int} = \frac{1}{2A}\left[\sum_{i=1}^{N}\left(\frac{p^2_{xi} + p^2_{yi}}{m}\right) - (2A)\frac{d\phi}{dA}\right]. \tag{B15}$$

The equations of motion were integrated by employing explicit reversible integrators using factorization techniques for the Liouville time evolution operator. We used the reversible reference system propagator algorithm (RESPA), which allows to define different time steps for the integration of fast and slow degrees of freedom [32].

APPENDIX C: SPINODAL RELATION

The stability condition of a 2D solid requires that the free energy F must be a convex function of its natural variables. In particular, $\partial^2 F/\partial A_p^2 > 0$. A mechanical instability appears at the area $A_{p,C}$ if [50–52]

$$\left(\frac{\partial^2 F}{\partial A_p^2}\right)_{A_{p,C}} = 0\,. \tag{C1}$$

The in-plane stress at the critical area is

$$\tau_C = -\left(\frac{\partial F}{\partial A_p}\right)_{A_{p,C}}. \tag{C2}$$

The Taylor expansion of F at the critical area $A_{p,C}$ is, under consideration of Eq. (C1) and up to the order $O[(A_p - A_{p,C})^4]$, given as

$$F = F_C - \tau_C(A_p - A_{p,C}) + a(A_p - A_{p,C})^3, \tag{C3}$$

where $F_C \equiv F(A_{p,C})$ and a is a constant proportional to the third A_p derivative of F at the critical area $A_{p,C}$. The in-plane stress is obtained by the derivative of the last equation as

$$\tau = \tau_C - 3a(A_p - A_{p,C})^2. \tag{C4}$$

From this equation,

$$A_p = A_{p,C} + \left(\frac{1}{3a}\right)^{1/2}(\tau_C - \tau)^{1/2}. \tag{C5}$$

By considering the definition of the 2D compressional modulus in Eq. (5) and with the help of Eqs. (C4) and (C5), one gets

$$B = (3a)^{1/2}A_{p,C}(\tau_C - \tau)^{1/2} + O(\tau_C - \tau), \tag{C6}$$

which gives us the dependence of the 2D compressional modulus B with the in-plane stress τ expected close to the spinodal instability of the layer at the critical stress τ_C. Our simulation results for $B(\tau)$ are in good agreement with the last equation.

[1] K. S. Novoselov, A. K. Geim, S. V. Morozov, D. Jiang, Y. Zhang, S. V. Dubonos, I. V. Grigorieva, and A. A. Firsov, Science **306**, 666 (2004).

[2] B. Amorim, A. Cortijo, F. de Juan, A. Grushin, F. Guinea, A. Gutiérrez-Rubio, H. Ochoa, V. Parente, R. Roldán, P. San-Jose, J. Schiefele, M. Sturla, and M. Vozmediano, Phys. Rep. **617**, 1 (2016).

[3] D. R. Cooper, B. D'Anjou, N. Ghattamaneni, B. Harack, M. Hilke, A. Horth, N. Majlis, M. Massicotte, L. Vandsburger, E. Whiteway, and V. Yu, ISRN Condens. Matter Phys. **2012**, 501686 (2012).

[4] N. D. Mermin and H. Wagner, Phys. Rev. Lett. **17**, 1133 (1966).

[5] J. H. Los, M. I. Katsnelson, O. V. Yazyev, K. V. Zakharchenko, and A. Fasolino, Phys. Rev. B **80**, 121405(R) (2009).

[6] B. Amorim, R. Roldán, E. Cappelluti, A. Fasolino, F. Guinea, and M. I. Katsnelson, Phys. Rev. B **89**, 224307 (2014).

[7] B. Pamuk, J. M. Soler, R. Ramírez, C. P. Herrero, P. W. Stephens, P. B. Allen, and M.-V. Fernández-Serra, Phys. Rev. Lett. **108**, 193003 (2012).

[8] N. Mounet and N. Marzari, Phys. Rev. B **71**, 205214 (2005).

[9] I. R. Storch, R. De Alba, V. P. Adiga, T. S. Abhilash, R. A. Barton, H. G. Craighead, J. M. Parpia, and P. L. McEuen, Phys. Rev. B **98**, 085408 (2018).

[10] C. P. Herrero and R. Ramírez, J. Chem. Phys. **148**, 102302 (2018).

[11] K. H. Michel, S. Costamagna, and F. M. Peeters, Phys. Status Solidi (b) **252**, 2433 (2015).
[12] G. Grimvall, *Thermophysial Properties of Materials* (Elsevier, Amsterdam, 1999).
[13] K. H. Michel, S. Costamagna, and F. M. Peeters, Phys. Rev. B **91**, 134302 (2015).
[14] V. Adamyan, V. Bondarev, and V. Zavalniuk, Phys. Lett. A **380**, 3732 (2016).
[15] V. N. Bondarev, V. M. Adamyan, and V. V. Zavalniuk, Phys. Rev. B **97**, 035426 (2018).
[16] J.-B. Fournier and C. Barbetta, Phys. Rev. Lett. **100**, 078103 (2008).
[17] H. Shiba, H. Noguchi, and J.-B. Fournier, Soft Matter **12**, 2373 (2016).
[18] P. L. Doussal and L. Radzihovsky, Ann. Phys. **392**, 349 (2018).
[19] W. Gao and R. Huang, J. Mech. Phys. Solids **66**, 42 (2014).
[20] R. Roldán, A. Fasolino, K. V. Zakharchenko, and M. I. Katsnelson, Phys. Rev. B **83**, 174104 (2011).
[21] J. H. Los, A. Fasolino, and M. I. Katsnelson, Phys. Rev. Lett. **116**, 015901 (2016).
[22] J. Hašík, E. Tosatti, and R. Martoňák, Phys. Rev. B **97**, 140301(R) (2018).
[23] R. Ramírez, E. Chacón, and C. P. Herrero, Phys. Rev. B **93**, 235419 (2016).
[24] J. H. Los, L. M. Ghiringhelli, E. J. Meijer, and A. Fasolino, Phys. Rev. B **72**, 214102 (2005).
[25] R. Ramírez and T. López-Ciudad, J. Chem. Phys. **115**, 103 (2001).
[26] R. Ramírez and C. P. Herrero, J. Chem. Phys. **151**, 224107 (2019).
[27] L. M. Ghiringhelli, J. H. Los, A. Fasolino, and E. J. Meijer, Phys. Rev. B **72**, 214103 (2005).
[28] K. V. Zakharchenko, M. I. Katsnelson, and A. Fasolino, Phys. Rev. Lett. **102**, 046808 (2009).
[29] A. Fasolino, J. H. Los, and M. I. Katsnelson, Nat. Mater. **6**, 858 (2007).
[30] L. M. Ghiringhelli, J. H. Los, E. J. Meijer, A. Fasolino, and D. Frenkel, Phys. Rev. Lett. **94**, 145701 (2005).
[31] A. Politano, A. R. Marino, D. Campi, D. Farías, R. Miranda, and G. Chiarello, Carbon **50**, 4903 (2012).
[32] G. J. Martyna, M. E. Tuckerman, D. J. Tobias, and M. L. Klein, Mol. Phys. **87**, 1117 (1996).
[33] C. P. Herrero and R. Ramírez, J. Phys.: Condens. Matter **26**, 233201 (2014).
[34] R. Ramírez and T. López-Ciudad, in *Quantum Simulations of Complex Many–Body Systems: From Theory to Algorithms*, edited by J. Grotendorst, D. Marx, and A. Muramatsu (NIC, FZ Jülich, 2002), p. 325.
[35] R. Ramírez and C. P. Herrero, Phys. Rev. B **72**, 024303 (2005).
[36] J. Zimmermann, P. Pavone, and G. Cuniberti, Phys. Rev. B **78**, 045410 (2008).
[37] P. L. de Andres, F. Guinea, and M. I. Katsnelson, Phys. Rev. B **86**, 144103 (2012).
[38] R. Ramírez and C. P. Herrero, Phys. Rev. B **97**, 235426 (2018).
[39] R. Ramírez and C. P. Herrero, J. Chem. Phys. **149**, 041102 (2018).
[40] R. Ramírez and C. P. Herrero, Phys. Rev. B **95**, 045423 (2017).
[41] F. Behroozi, Langmuir **12**, 2289 (1996).
[42] X. Cong, Q.-Q. Li, X. Zhang, M.-L. Lin, J.-B. Wu, X.-L. Liu, P. Venezuela, and P.-H. Tan, Carbon **149**, 19 (2019).
[43] L. D. Landau and E. M. Lifshitz, *Statistical Physics*, 3rd ed. (Pergamon, Oxford, 1980).
[44] D. Tisi, Master's thesis, Università di Modena e Reggio Emilia, 2017.
[45] P. Lambin, Appl. Sci. **4**, 282 (2014).
[46] G. J. Martyna and M. L. Klein, J. Chem. Phys. **97**, 2635 (1992).
[47] G. J. Martyna, D. J. Tobias, and M. L. Klein, J. Chem. Phys. **101**, 4177 (1994).
[48] M. E. Tuckerman and A. Hughes, in *Classical & Quantum Dynamics in Condensed Phase Simulations*, edited by B. J. Berne and D. F. Coker (World Scientific, Singapore, 1998), p. 311.
[49] G. J. Martyna, A. Hughes, and M. E. Tuckerman, J. Chem. Phys. **110**, 3275 (1999).
[50] H. J. Maris, Phys. Rev. Lett. **66**, 45 (1991).
[51] J. Boronat, J. Casulleras, and J. Navarro, Phys. Rev. B **50**, 3427 (1994).
[52] C. P. Herrero, Phys. Rev. B **68**, 172104 (2003).